Architecture and assembly of the archaeal Cdc48·20S proteasome

Dominik Barthelme[a,1], James Z. Chen[a,1,2], Jonathan Grabenstatter[b], Tania A. Baker[a,c], and Robert T. Sauer[a,3]

Departments of [a]Biology and [b]Earth and Planetary Sciences and [c]Howard Hughes Medical Institute, Massachusetts Institute of Technology, Cambridge, MA 02139

ATP-dependent proteases maintain protein quality control and regulate diverse intracellular functions. Proteasomes are primarily responsible for these tasks in the archaeal and eukaryotic domains of life. Even the simplest of these proteases function as large complexes, consisting of the 20S peptidase, a barrel-like structure composed of four heptameric rings, and one or two AAA+ (ATPase associated with a variety of cellular activities) ring hexamers, which use cycles of ATP binding and hydrolysis to unfold and translocate substrates into the 20S proteolytic chamber. Understanding how the AAA+ and 20S components of these enzymes interact and collaborate to execute protein degradation is important, but the highly dynamic nature of prokaryotic proteasomes has hampered structural characterization. Here, we use electron microscopy to determine the architecture of an archaeal Cdc48·20S proteasome, which we stabilized by site-specific cross-linking. This complex displays coaxial alignment of Cdc48 and 20S and is enzymatically active, demonstrating that AAA+ unfoldase wobbling with respect to 20S is not required for function. In the complex, the N-terminal domain of Cdc48, which regulates ATP hydrolysis and degradation, packs against the D1 ring of Cdc48 in a coplanar fashion, constraining mechanisms by which the N-terminal domain alters 20S affinity and degradation activity.

AAA+ protease | dynamic wobbling model | p97/VCP

Proteasomes are large macromolecular complexes that degrade misfolded or damaged proteins to maintain cellular homeostasis and quality control in all domains of life. In addition, selective proteasomal turnover of regulatory proteins is often a critical element of signaling cascades that allow cells to respond to changing conditions and environmental stress (1, 2). Proteasomes consist of the self-compartmentalized 20S peptidase and one or two AAA+ (ATPase associated with a variety of cellular activities) family ring hexamers. The $\alpha_7\beta_7\beta_7\alpha_7$ ring topology of the 20S enzyme ensures that the proteolytic active sites, which reside in the β-subunits, are sequestered and can only cleave substrates that enter the chamber through narrow axial pores formed by the α-subunits (3). As a consequence, ATP-dependent unfolding of natively folded protein substrates by the AAA+ ring and subsequent polypeptide translocation through a narrow axial channel and into the 20S chamber are required for degradation (4).

Although the 20S peptidase is the degradation module in all proteasomes, the associated AAA+ unfolding machines differ. For example, homohexamers of Mpa/Arc in actinobacteria and PAN in archaea serve as proteasomal motors, whereas a heterohexameric Rpt_{1-6} ring in the 19S particle is the motor of the eukaryotic 26S proteasome (2, 5). Characteristic of type-I AAA+ enzymes, Mpa/Arc, PAN, and Rpt_{1-6} subunits contain a single AAA+ module for ATP binding and hydrolysis (6). By contrast, as found in type-II AAA+ enzymes, the homohexameric Cdc48 motor in the recently discovered archaeal Cdc48·20S proteasome contains two AAA+ modules (7, 8). Cdc48 is essential in archaea and eukaryotes, and structural studies of a mouse ortholog have shown that its AAA+ modules are organized into discrete D1 and D2 rings (9–11). Cdc48 also contains a family-specific N domain, as well as a flexible C-terminal sequence, including an HbYX

(hydrophobic, tyrosine, any residue) tripeptide important for 20S binding, which is similar to motifs in Mpa/Arc, Pan, and Rpt_{1-6} (8). Electron microscopy (EM) has been used to probe the structures of the PAN·20S archaeal proteasome and the 26S eukaryotic proteasome (12, 13). These EM studies showed that many unfoldase rings did not align coaxially with 20S, despite making contact with the peptidase α-ring, resulting in wobbling distances as large as 30 Å. It was proposed that as ATP hydrolysis progresses in the PAN and Rpt_{1-6} rings, wobbling motions arise because the HbYX tails of newly ATP-bound subunits interact with binding pockets in the 20S α-subunit, whereas HbYX motifs in posthydrolytic subunits assume a nonbinding conformation (14). However, recent EM studies have shown that the rings of Rpt_{1-6} and 20S shift into more symmetric and coaxially aligned positions upon substrate engagement, questioning the functional importance of dynamic wobbling (15).

Eukaryotic Cdc48 (also known as p97 or VCP) plays crucial roles in diverse cell functions, many involving the ubiquitin–proteasome system and adaptor proteins that bind to the N domain of Cdc48 (9). In some structures, the N domain packs against the D1 ring; in other structures, it adopts positions above or below the D1 ring or is disordered (16–18). Because these movements correlate with bound nucleotide or the presence of human-disease mutations, N-domain movements are thought to be important for regulating Cdc48 function. In archaeal Cdc48, deletion of the N domain increases 20S-binding affinity, increases rates of ATP hydrolysis, and increases unfolding/degradation activity (8, 19). Breaking contacts between the N domain and the

Significance

From microbes to humans, proteolytic machines called proteasomes cleave proteins that are damaged or unnecessary into peptide fragments. Proteasomes minimally consist of the barrel-like 20S peptidase and an AAA+ ring, which harnesses chemical energy to unfold and translocate proteins into the 20S chamber for degradation. Here, we determine the architecture of a recently discovered proteasome, Cdc48·20S, by electron microscopy. A continuous axial channel allows translocation through the double AAA+ rings of Cdc48 into the 20S chamber. A model in which dynamic "wobbling" of the AAA+ unfoldase relative to 20S is necessary for function is ruled out for Cdc48·20S by electron-microscopy results showing coaxial alignment of Cdc48 and 20S and by the proteolytic activity of cross-linked complexes.

www.manaraa.com

D1 ring might therefore be required for tight binding of Cdc48 to the 20S peptidase and for enhanced activity.

Here, we determine EM structures of archaeal Cdc48–20S and Cdc48$^{\Delta N}$–20S proteasomes, in which the C-terminal tails of Cdc48 were cross-linked to specific sites in the α ring of 20S. Importantly, the cross-linked complexes are highly active in protein unfolding and degradation. Although the resolution of both structures is low, several features are clear. First, the Cdc48 and 20S rings are co-axially aligned. In combination with the activity of cross-linked complexes, this result supports a model in which wobbling motions are not required to allow protein degradation. Second, in the Cdc48–20S structure, the N domain is packed in a coplanar manner against the D1 ring. We discuss the implications of these results in terms of current understanding of Cdc48 and proteasomal structure and function.

Results and Discussion

Nucleotide Effects on Complex Stability. We previously found that *Thermoplasma acidophilum* Cdc48·20S and Cdc48$^{\Delta N}$·20S proteasomes assemble in an ATP-dependent manner with apparent binding constants of ~160 and ~3 nM, respectively, but pull-down experiments suggested that both complexes had relatively short half-lives (8). Prior studies showed that complexes of *T. acidophilum* 20S with PAN from another archaeal genus were also kinetically unstable, and EM studies of this proteasome were only possible by using adenosine 5′-gamma-thiotriphosphate (ATPγS), a nucleotide analog that was not hydrolyzed (13, 14). As a prelude to structural studies, we investigated whether more stable Cdc48·20S complexes could be obtained using ATP analogs. Surprisingly, however, Cdc48$^{\Delta N}$ bound 20S far less tightly in the presence of 2 mM ATPγS (K_{app} ~ 700 nM) than in the presence of 2 mM ATP (K_{app} ~ 3 nM), as assayed by stimulation of peptide cleavage (Fig. 1A). Indeed, we previously reported that ATPγS did not support Cdc48 binding to 20S in a similar assay, which was probably a consequence of very weak binding at the enzyme concentrations used. We found that ADP·AlF$_4^-$, a transition-state analog, also supported a functional interaction between Cdc48$^{\Delta N}$ and the 20S peptidase (Fig. 1B), but titration experiments revealed that binding (K_{app} ~ 270 nM) was again much weaker than observed with ATP (Fig. 1C). We also assayed the 20S affinity of a Cdc48$^{\Delta N}$ variant (E291Q/E568Q) that cannot hydrolyze ATP rapidly because of mutations in the
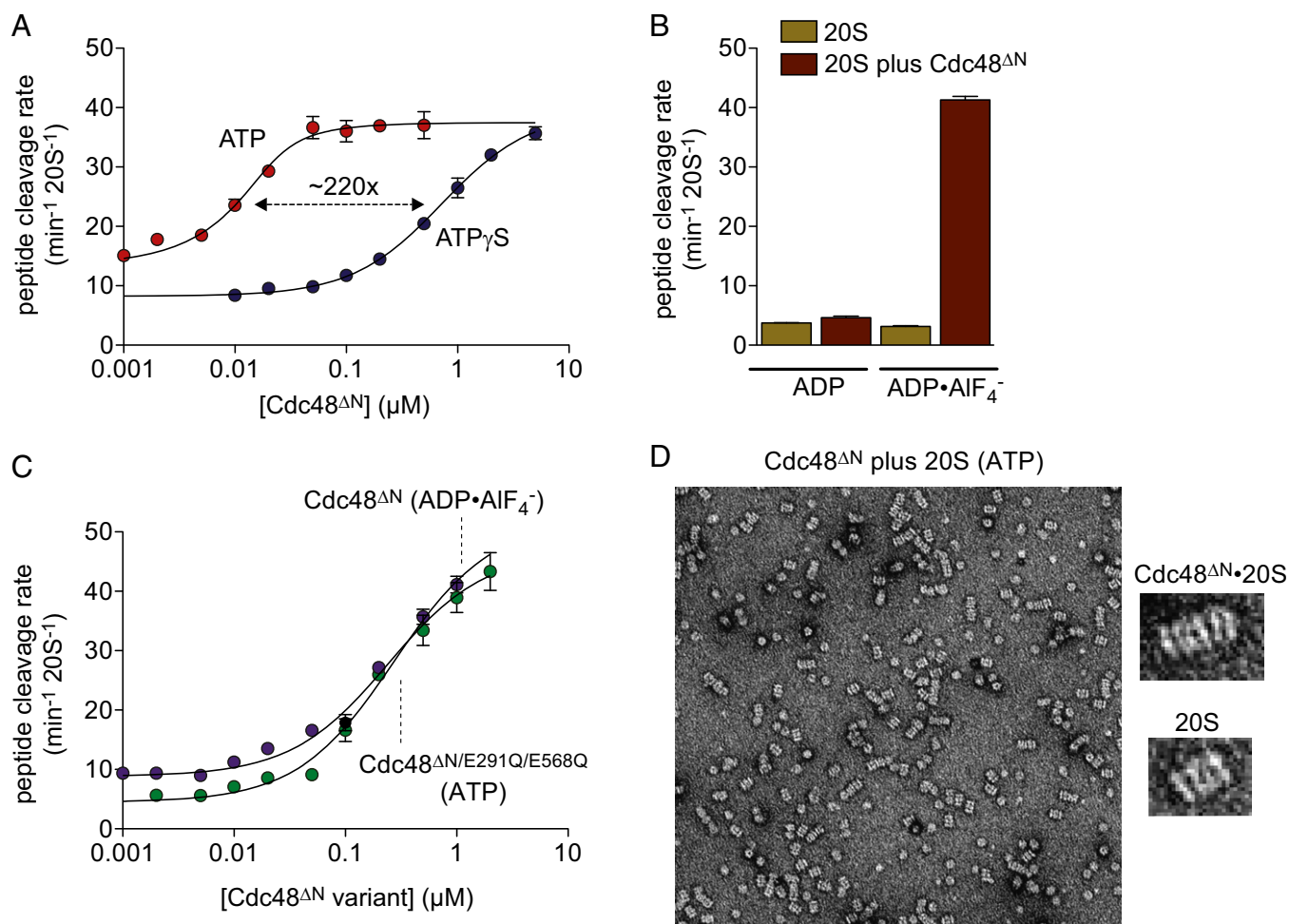

Fig. 1. Nucleotide dependence of assembly. (*A*) Stimulation of nonapeptide (10 μM) cleavage by the 20S peptidase (10 nM) as a function of increasing Cdc48$^{\Delta N}$ in the presence of 2 mM ATP or ATPγS. Values are averages ± SEM (*n* = 3). Lines are fits to a quadratic equation for near-stoichiometric binding (ATP) or a one-site binding isotherm (ATPγS). Fitted K_{app} values were 3 ± 1 nM (ATP) and 702 ± 9 nM (ATPγS). (*B*) Cdc48$^{\Delta N}$ (1 μM) activates 20S (10 nM) cleavage of the nonapeptide (10 μM) in the presence of 2 mM ADP·AlF$_4^-$ but not ADP. Values are averages ± SEM (*n* = 3). (*C*) Stimulation of nonapeptide (10 μM) cleavage by the 20S peptidase (10 nM) as a function of increasing Cdc48$^{\Delta N}$ (in the presence of 2 mM ADP·AlF$_4^-$; K_{app} = 270 ± 30 nM) or Cdc48$^{\Delta N/E291Q/E568Q}$ (in the presence of 2 mM ATP; K_{app} = 240 ± 34 nM). Values are averages ± SEM (*n* = 3). Lines are fits to a one-site binding isotherm. (*D*) Representative examples of negative-stained micrographs of Cdc48$^{\Delta N}$ plus 20S in the presence of 2 mM ATP. *Right* shows an assembled Cdc48$^{\Delta N}$·20S complex (observed in ~10–20% of particles) and a particle of 20S alone.

www.manaraa.com

Walker-B ATPase motifs of the D1 and D2 rings. This protein also bound 20S binding relatively weakly in the presence of ATP ($K_{app} \sim 240$ nM) (Fig. 1C). In combination, these results show that ATP supports the highest affinity of Cdc48$^{\Delta N}$ for 20S and suggest that strong 20S affinity requires ATP binding and hydrolysis by Cdc48.

In negative-stain EM images of mixtures of 20S, Cdc48$^{\Delta N}$ or Cdc48, and ATP, we observed 10–20% complexes with Cdc48$^{\Delta N}$ (Fig. 1D) but almost no complexes with Cdc48, making structure determination infeasible. To overcome this problem, we developed a site-specific cross-linking procedure as described below.

Cross-Linked Complexes. We initially generated cysteine-free variants of *T. acidophilum* Cdc48 (C77A/C679A; designated Cdc48*) and 20S (αC151S; designated 20S*). Cdc48* was as active as wild-type Cdc48 in ATP hydrolysis, protein unfolding, and protein

degradation (Fig. 2A), and 20S* was as active as wild-type 20S in peptide cleavage (Fig. 2B). We then introduced a cysteine (L745C) at the X position of the C-terminal HbYX tripeptide of Cdc48*, because these residues are hypothesized to dock into a binding cleft in the 20S α ring (8, 20). We introduced another cysteine (K66C) into the hydrophobic cleft of the α-subunit of 20S*. Attempts to form disulfide bonds between Cdc48*/L745C and 20S*/K66C by using copper-1,10-phenanthroline or 5,5'-dithiobis-2-nitrobenzoic acid (DTNB) were complicated by intramolecular cross-linking between Cdc48 protomers. However, reacting 20S*/K66C with 1,2-bis(maleimide)ethane (BMOE) followed by the addition of substoichiometric Cdc48*/L745C or Cdc48*/ΔN/L745C resulted in cross-linking yields of 50% or more (Fig. 2C). Because there are six potential sites of cross-linking, almost every complex contained at least one cross-link. Excess 20S*/K66C that was not cross-linked to Cdc48*/L745C or Cdc48*/ΔN/L745C was removed
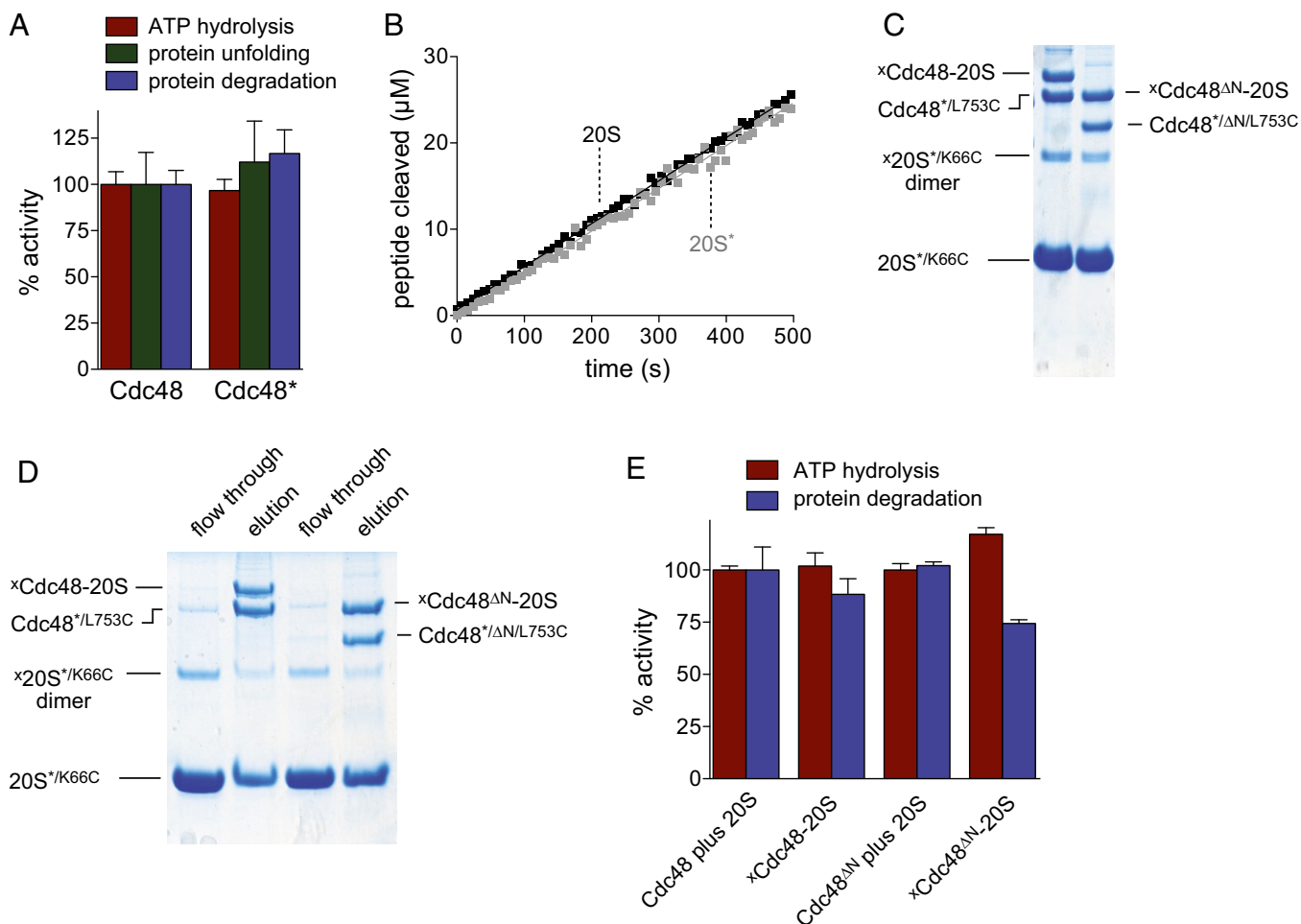
Fig. 2. Cross-linked Cdc48–20S complexes are functional. (A) Rates of ATP hydrolysis, Kaede–ssrA unfolding, and ^{SF}GFP–ssrA degradation were determined at 45 °C for the cysteine-free Cdc48* variant and were normalized to Cdc48 values. Values are averages ± SEM ($n = 3$). Hydrolysis of ATP (2 mM) by Cdc48 or Cdc48* (0.3 μM) was measured in the presence of an ATP-regeneration system. Unfolding of Kaede–ssrA (10 μM) by Cdc48 or Cdc48* (1 μM) and degradation of ^{SF}GFP–ssrA (10 μM) by Cdc48 or Cdc48* (1 μM) plus 20S (3 μM) was measured in the presence of 10 mM ATP and a regeneration system. Rates of ATP hydrolysis were 22 ± 0.29 min^{-1}·enzyme (enz)$^{-1}$ (Cdc48) and 20 ± 0.69 min^{-1}·enz^{-1} (Cdc48*). Rates of Kaede–ssrA unfolding were 0.011 ± 0.002 min^{-1}·enz^{-1} (Cdc48) and 0.013 ± 0.002 min^{-1}·enz^{-1} (Cdc48*). Rates of ^{sf}GFP–ssrA degradation were 0.014 ± 0.001 min^{-1}·enz^{-1} (Cdc48·20S) and 0.016 ± 0.004 min^{-1}·enz^{-1} (Cdc48*·20S). (B) Cleavage of the tetrapeptide Suc-LLVY-Amc (100 μM) by 20S or 20S* (0.2 μM) was assayed at 45 °C. (C) Reducing SDS/PAGE gel following BMOE cross-linking of Cdc48*/L745C or Cdc48*/ΔN/L745C (2 μM) to 20S*/K66C (12 μM). The positions of non-cross-linked reactants and cross-linked ^{x}Cdc48–20S, ^{x}Cdc48$^{\Delta N}$–20S, and a ^{x}20S*/K66C dimer are shown. (D) Reducing SDS/PAGE following removal of excess non-cross-linked 20S*/K66C by affinity purification using Strep-Tactin resin. (E) Rates of ATP hydrolysis and ^{SF}GFP–ssrA degradation by cross-linked ^{x}Cdc48–20S or ^{x}Cdc48$^{\Delta N}$–20S (1 μM) relative to Cdc48 or Cdc48$^{\Delta N}$ (1 μM) plus 20S (3 μM). Reactions were performed as described in A. Rates of ATP hydrolysis were 22 ± 1 min^{-1}·enz^{-1} (Cdc48·20S), 21 ± 1 min^{-1}·enz^{-1} (^{x}Cdc48–20S), 245 ± 7 min^{-1}·enz^{-1} (Cdc48$^{\Delta N}$·20S), and 287 ± 7 min^{-1}·enz^{-1} (^{x}Cdc48$^{\Delta N}$–20S). Rates of degradation were 0.013 ± 0.002 min^{-1}·enz^{-1} (Cdc48·20S), 0.013 ± 0.002 min^{-1}·enz^{-1} (^{x}Cdc48–20S), 0.97 ± 0.017 min^{-1}·enz^{-1} (Cdc48$^{\Delta N}$·20S), and 0.71 ± 0.016 min^{-1}·enz^{-1} (^{x}Cdc48$^{\Delta N}$–20S).

BIOCHEMISTRY

by using an affinity purification (Fig. 2D). Below, we refer to these cross-linked complexes as ^{x}Cdc48–20S or ^{x}Cdc48^{ΔN}–20S.

Importantly, purified ^{x}Cdc48–20S and ^{x}Cdc48^{ΔN}–20S hydrolyzed ATP and degraded a stable native protein at rates similar to the noncovalent complexes (Fig. 2E). ^{x}Cdc48–20S supported peptide cleavage at a higher rate than Cdc48 plus 20S (Fig. S1). Thus, cross-linking does not prevent protein unfolding by Cdc48, Cdc48-mediated translocation of substrates into 20S, or 20S proteolysis.

Cdc48–20S EM Structure. In negative-stain EM images, ^{x}Cdc48^{ΔN}–20S particles preferentially assumed side-view orientations (Fig. 3A). The 2D class averages for ^{x}Cdc48^{ΔN}–20S and ^{x}Cdc48–20S particles clearly showed the overall architecture and interaction between the Cdc48 double ring and the $α_7β_7β_7α_7$ rings of 20S (Fig. 3B). ^{x}Cdc48–20S had a width of ~16 nm and a height of ~24 nm. As a consequence of the enzyme stoichiometries during cross-linking, the vast majority of complexes consisted of 20S capped by a single Cdc48 or Cdc48^{ΔN} hexamer, whereas <1% doubly capped complexes were observed. As described in *Materials and Methods*, 3D reconstruction yielded electron-density maps for ^{x}Cdc48–20S and ^{x}Cdc48^{ΔN}–20S at resolutions of ~40 Å (Fig. 3C). Crystal structures of *T. acidophilum* 20S [Protein Data Bank (PDB) ID code 1PMA] and mouse Cdc48/p97 (PDB ID code 3CF1) could be rigid-body-fitted into the density maps reasonably well (Fig. 3D).

In ~90% of ^{x}Cdc48–20S and ^{x}Cdc48^{ΔN}–20S images, the double ring of the Cdc48 hexamer aligned coaxially with the $α_7β_7β_7α_7$ rings of 20S. There were, however, images in which the Cdc48 rings were tilted relative to the 20S rings (Fig. 3 E, Left), potentially resulting from incomplete cross-linking and partial dissociation. As noted above, this wobbling phenomenon was reported as a prominent feature for PAN·20S and the 26S proteasome (12, 13). In the 2D classes, the shared portions of ^{x}Cdc48–20S and ^{x}Cdc48^{ΔN}–20S were highly similar (Fig. 3B). In the 3D structures
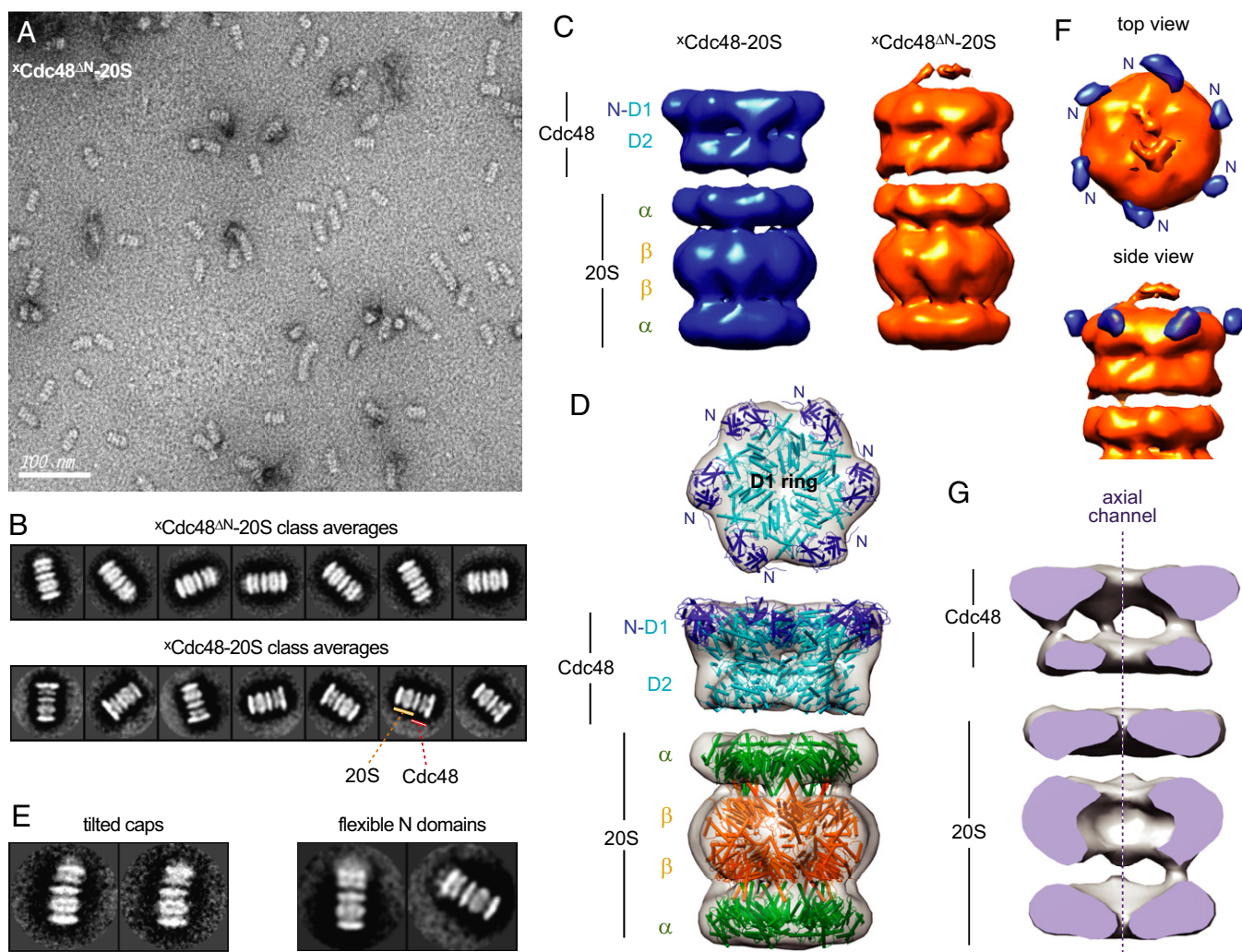
Fig. 3. Negative-stain EM structures of the ^{x}Cdc48–20S and ^{x}Cdc48^{ΔN}–20S proteasomes. (A) Representative electron micrograph of cross-linked ^{x}Cdc48^{ΔN}–20S particles showing assembled complexes as the dominant species. (B) Representative class averages for ^{x}Cdc48^{ΔN}–20S proteasomes (*Upper*) and ^{x}Cdc48–20S proteasomes (*Lower*). (C) Shown are 3D reconstructions of the ^{x}Cdc48–20S (*Left*) and ^{x}Cdc48^{ΔN}–20S (*Right*) proteasomes. (D) The crystal structures of mouse Cdc48/p97 (PDB ID code 3CF1) and *T. acidophilum* 20S (PDB ID code 1PMA) in cartoon representation fit well into the ^{x}Cdc48–20S electron-density map, as shown in top and side views. In the Cdc48 structure, the N domains are colored dark blue, and the D1 and D2 rings are colored cyan. In the 20S structure, the α rings are colored green and the β rings are colored orange. (E, Left) Some class averages of ^{x}Cdc48^{ΔN}–20S particles (~10% of total) did not show coaxial alignment of Cdc48 and 20S. (Right) In a few ^{x}Cdc48–20S particles, the N domain had moved from its coplanar position to a position above the D1 AAA+ ring or was generally flexible. (F) A 3D difference map of ^{x}Cdc48–20S and ^{x}Cdc48^{ΔN}–20S localized the N domain (blue) to a position coplanar to the D1 ring. (G) Cutaway of the electron-density map of ^{x}Cdc48–20S showing a continuous axial channel through the rings of Cdc48 and 20S.

www.manaraa.com

(Fig. 3C), the D2 ring also assumed a fixed position with respect to 20S, suggesting that there is relatively little flexibility in the complex. On the outer edge and coplanar with the D1 ring, well-defined density was observed in ^{x}Cdc48–20S, but not ^{x}Cdc48$^{\Delta N}$–20S, both in 2D classes and the 3D reconstruction, which we assigned as the N domain (Fig. 3 D and F). In <5% of all ^{x}Cdc48–20S classes, the N domain was observed at a position above the D1 ring, or density was missing (Fig. 3 E, Right), suggesting disorder. In the 3D reconstructions of ^{x}Cdc48$^{\Delta N}$–20S and ^{x}Cdc48–20S, the $\alpha_7\beta_7\beta_7\alpha_7$ rings of 20S were unequivocally identified, and the α_7 ring proximal to Cdc48 had a larger diameter than the distal α_7 ring (Fig. 3 C and D). This difference presumably reflects changes needed to accommodate docking, but could also be a consequence of allosteric communication between Cdc48 and 20S. At the resolution of the structure, a continuous axial channel passed through the D1 and D2 rings of Cdc48 and the α and β rings of 20S (Fig. 3G).

In the 3D reconstruction of ^{x}Cdc48$^{\Delta N}$–20S, weak electron density was observed on top and near the axis of the D1 ring (Fig. 3 C and F and Fig. S2), but the source of this additional density is uncertain. Possibilities include density from a conformational change in some D1 AAA+ rings; density from the N-terminal affinity tag, which is located near this position; and/or density from a heterogeneous population of Cdc48$^{\Delta N}$ polypeptide in the process of being degraded, because ATP-dependent autodegradation of the Cdc48$^{\Delta N}$ subunit by Cdc48$^{\Delta N}$·20S was observed (Fig. S3). This extra density was not observed in the ^{x}Cdc48–20S structure (Fig. 3C and Fig. S2), and no significant autodegradation was detected for Cdc48·20S (Fig. S3).

Regulation of Cdc48 Activity and 20S Binding by the N Domain. For archaeal Cdc48, EM studies suggested that the N domain might be flexible or extend away from the D1 ring, and deletion of the N domain enhances ATP hydrolysis, protein unfolding, and protein degradation, and strengthens 20S affinity (8, 19, 21, 22). For eukaryotic Cdc48/p97, the N domain moves above or below the D1 ring, depending upon the nucleotide state and the presence of human-disease mutations, and locking the N domain to the D1 via a disulfide bond abrogates ATP hydrolysis (16–18, 23). These results are consistent with a model in which packing of the N domain against the D1 ring negatively regulates multiple Cdc48 activities, and we anticipated that the N domain might be disordered in the complex of archaeal Cdc48 with 20S. In almost all Cdc48–20S complexes, however, the N domain packed against the D1 ring in a coplanar fashion (Fig. 3 A and C). Thus, packing of the N domain against the D1 ring is compatible with 20S binding, even it these contacts alter Cdc48/p97 activity and 20S binding affinity.

To determine the effects of disulfide locking the archaeal N domain to the D1 ring, we constructed Cdc48$^{P138C/N373C}$ based on homology and the previous p97 experiments (23). After oxidation with copper-1,10-phenanthroline, disulfide-bond formation was 50–80% complete, depending on the nucleotide (Fig. 4A). Compared with Cdc48*, reduced Cdc48$^{*/P138C/N373C}$ was approximately twofold less active in ATP hydrolysis, and oxidized Cdc48$^{*/P138C/N373C}$ was approximately sixfold less active (Fig. 4B). Reduced Cdc48$^{*/P138C/N373C}$ bound 20S with essentially the same affinity as Cdc48*, whereas oxidized Cdc48$^{*/P138C/N373C}$ bound 20S substantially more weakly (Fig. 4C). We conclude that the exact nature of interactions between the N domain and the D1 ring affect ATP hydrolysis but do not preclude 20S binding, consistent with our EM structures. What then accounts for the ~100-fold increase in 20S affinity and enhanced activity when the N domain of archaeal Cdc48 is deleted? We assume that there must be modest conformational changes in Cdc48$^{\Delta N}$ and its interface with the 20S α ring that are not evident at the low resolution of our EM structures.
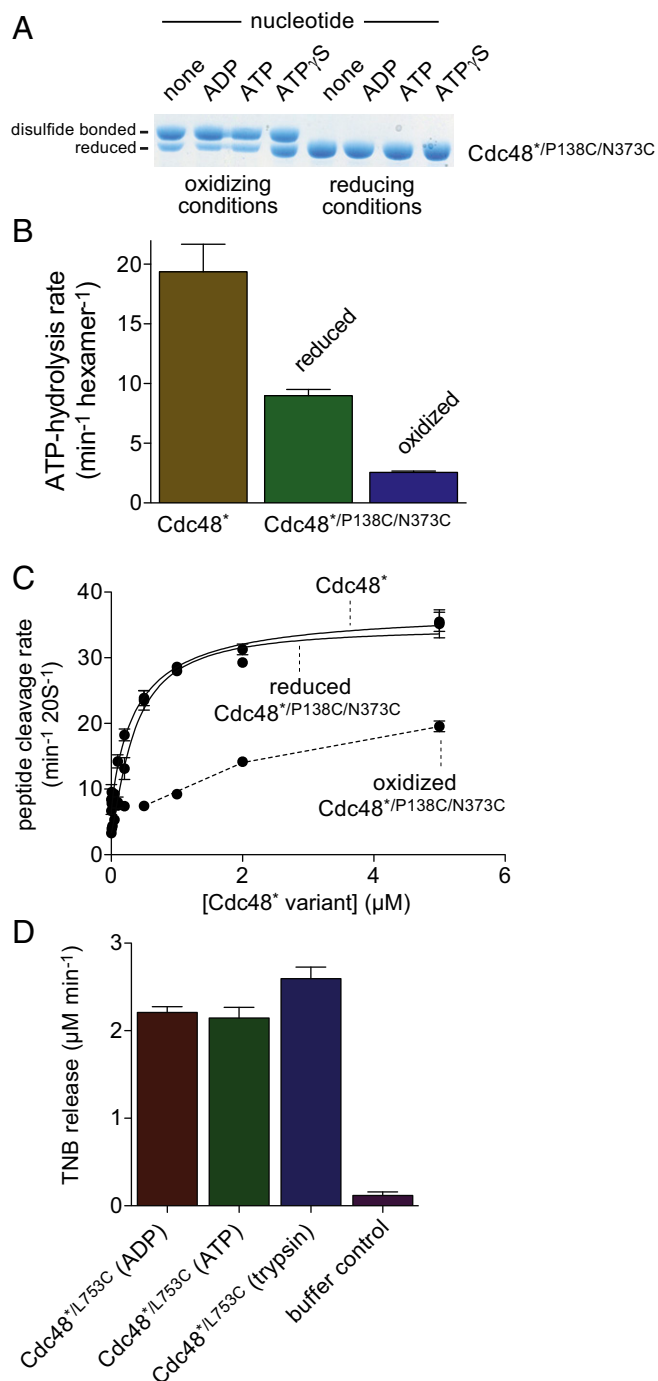
Fig. 4. Role of contacts between the N domain and D1 ring in ATP hydrolysis and 20S binding and experiments probing accessibility of the HbYX tails. (A) Nonreducing SDS/PAGE of Cdc48$^{*/P138C/N373C}$ following incubation with copper-1,10-phenanthroline (10 μM) in the presence of different nucleotides (2 mM) or no nucleotide (oxidizing conditions) or following oxidation and subsequent incubation with 10 mM DTT (reducing conditions). (B) Rates of ATP hydrolysis by reduced and oxidized Cdc48$^{*/P138C/N373C}$. Values are averages ± SEM (n = 3). Experiments were performed at 45 °C using 5 mM ATP, a regeneration system, and 5 μM Cdc48 variant. (C) Stimulation of nonapeptide (10 μM) cleavage by 20S (10 nM) as a function of increasing concentrations of Cdc48* or oxidized or reduced Cdc48$^{*/P138C/N373C}$. Values are averages ± SEM (n = 3) and were fit to a one-site binding isotherm. K_{app} values were 358 ± 41 nM (Cdc48*), 379 ± 57 nM (reduced Cdc48$^{*/P138C/N373C}$), and >2 μM (oxidized Cdc48$^{*/P138C/N373C}$). (D) Accessibility of the HbYX tail was probed by modification of the C-terminal Cys^{745} in Cdc48$^{*/L745C}$ with DTNB in the presence of ADP or ATP (2 mM) or following digestion of Cdc48$^{*/L745C}$ with trypsin.

Barthelme et al.

www.manaraa.com

Wobbling Does Not Appear to Be Functionally Important. Based on PAN·20S and early 26S proteasome EM studies, the AAA+ unfolding ring was proposed to wobble relative to the 20S peptidase, with an ordered sequence of ATP binding and hydrolysis resulting in conformational changes in the C-terminal tails that result in sequential making and breaking of contacts between the HbYX motifs and the 20S α ring (12–14). This model has been challenged by recent high-resolution cryo-EM structures of substrate-bound 26S proteasome, which show almost perfect coaxial alignment of the AAA+ Rpt_{1-6} ring and the 20S $\alpha_7\beta_7\beta_7\alpha_7$ rings (15, 24). Our results show coaxial alignment of the Cdc48 AAA+ rings with the 20S rings and establish that cross-linked complexes are active proteases. Collectively, these results imply that wobbling is not a general requirement for those proteasomal complexes and suggest that it may largely be an artifact of the kinetic instability of 20S complexes with AAA+ unfolding rings.

We found that a cysteine introduced at the C terminus of the HbYX motif in Cdc48$^{*/L745C}$ reacted with DTNB at similar rates in the presence of ATP or ADP and after cleavage of this protein with trypsin (Fig. 4D). These results suggest that nucleotide binding to Cdc48 does not change the accessibility of the HbYX motif substantially and thus is unlikely to control 20S binding by this mechanism. Previous studies have shown that the pore two loops of the Cdc48 D2 ring also contribute to 20S binding (7), and nucleotide-dependent changes in the D2 ring and these loops, which directly follow the Walker-B motif for ATP hydrolysis, may account for the ATP requirement for high-affinity 20S binding.

Potential Roles of ATP Hydrolysis in Cdc48 Binding to 20S. We found that ATPγS and ADP·AlF$_4^-$ support Cdc48$^{\Delta N}$ binding to the 20S peptidase, but with much weaker affinities than observed with ATP, suggesting that ATP hydrolysis is important for Cdc48 to form a high-affinity complex with 20S. Consistently, in the presence of ATP, the ATPase-defective Cdc48$^{\Delta N/E291Q/E568Q}$ variant binds the 20S peptidase ~100-fold more weakly than Cdc48$^{\Delta N}$. Although the mechanism by which ATP hydrolysis strengthens binding remains to be elucidated, we suggest two simple possibilities. In the first model, the D2 ring might assume a conformation following partial or complete ATP hydrolysis that could make additional or better contacts with 20S, but the lifetime of this high-affinity conformation is transient, and it decays rapidly unless there is ongoing ATP hydrolysis in both the D1 and D2 rings. In the second model, Cdc48 rings with a mixture of bound ATP and ADP might assume conformations with the highest 20S affinity. Indeed, such behavior was reported for the PAN·20S proteasome, although ATP is inferior to ATPγS in supporting high-affinity binding of PAN to 20S (14).

Mechanism of Protein Remodeling. An early crystal structure showed that the axial pore of Cdc48 was blocked by a metal ion, and many models of mechanical function were therefore proposed that do not involve polypeptide translocation (11). However, our findings that archaeal Cdc48 and variants of mammalian Cdc48/p97 function with the 20S peptidase in protein degradation strongly support a translocation model (7, 8). Our structures, which show a continuous axial channel through the D1, D2, and 20S α- and β-rings (Fig. 3G), provide additional support for this model. In this regard, we note that there is also strong evidence that the double-ring ClpB and Hsp-104 disaggregation chaperones operate by using translocation mechanisms (25, 26). Although these results do not rule out alternative models, we believe that many mechanical remodeling functions of Cdc48/p97 can be explained by a polypeptide-translocation mechanism.

Materials and Methods

Cloning, Expression, and Protein Purification. *T. acidophilum* Cdc48 mutants were generated by site-directed mutagenesis with Phusion DNA polymerase (New England Biolabs) using N-terminal His$_6$TEV-tagged Cdc48 in pET22b as a template (8). The endogenous C77 and C679 residues were mutated to

alanine to create cysteine-free Cdc48*. For cross-linking to 20S, we constructed a Cdc48$^{*/L745C}$ variant in which the His$_6$TEV tag was replaced with the MWSHPQFEKGGS sequence (StrepII tag and GGS linker). To create cysteine-free 20S*, the endogenous C151 residue in the *T. acidophilum* 20S α-subunit was replaced by serine and a C-terminal His$_6$ tag was added to the β-subunit. For N-domain disulfide locking experiments, we introduced the P138C and N373C mutations into Cdc48*.

Cdc48 and 20S variants were expressed in *E. coli* BL21-RIL cells as described (8). Proteins were initially purified by affinity chromatography on Strep-Tactin Superflow resin (Qiagen) or Ni^{2+}-NTA resin (Thermo Scientific), in the presence of 1 mM DTT and 1 mM EDTA. Proteins were then dialyzed against 20 mM Tris·HCl, 50 mM NaCl, 5 mM EDTA, and 1 mM DTT, loaded onto a MonoQ anion-exchange chromatography column (GE Healthcare), and eluted by applying a linear salt gradient to 600 mM NaCl. Proteins were concentrated by Amicon centrifugation devices (100-kDa cutoff; Millipore) and further purified by size-exclusion chromatography on a Superdex S-200 column (GE Healthcare) in 20 mM Hepes–KOH (pH 7.5), 50 mM NaCl, 1 mM DTT, and 1 mM EDTA. ^{SF}GFP-ssrA and Kaede-ssrA were expressed and purified as described (27, 28). All proteins were frozen in liquid nitrogen and stored at −80 °C. Protein concentrations were determined by UV-visible absorption and are reported as Cdc48 hexamer equivalents or 20S $\alpha_7\beta_7\beta_7\alpha_7$ equivalents.

Protein Cross-Linking. Residues suitable for cross-linking Cdc48 to 20S were identified by analyzing PA26-bound 20S structures (PDB ID codes 3JRM, 1YA7, and 3IPM) using the program Disulfide by Design (20, 29–31). For EM structural analyses, we cross-linked Cdc48$^{*/\Delta N/L745C}$ to 20S$^{*/K66C}$ and cross-linked Cdc48$^{*/L745C}$ to 20S* bearing αK33C and βT1A mutations. Before cross-linking, the 20S and Cdc48 proteins were buffer-exchanged twice into desalting buffer (20 mM Tris·HCl, pH 8.0, 100 mM NaCl, 1 mM EDTA) by using Micro-Spin columns (Bio-Rad) to remove DTT from the storage buffer. The 20S* variants were activated by incubation with 5 mM BMOE (Thermo Scientific) for 30 min at room temperature after lowering the pH to 6.5. Unreacted BMOE was removed from 20S by buffer exchange, and ^{x}Cdc48–20S complexes were formed by mixing 2 μM Cdc48 variants with 12 μM activated 20S by incubation in cross-linking buffer (100 mM Hepes–KOH, pH 6.5, 100 mM NaCl, 20 mM MgCl$_2$ 5 mM EDTA, and 5 mM ATP) at 37 °C for 2 h. Reactions were stopped by adding 10 mM iodoacetic acid, and cross-linking was analyzed by SDS/PAGE followed by staining with Coomassie blue. ^{x}Cdc48–20S complexes were further purified on Strep-Tactin resin (Qiagen) to remove non-cross-linked 20S.

To lock the N domain and D1 ring with a disulfide, the Cdc48$^{*/P138C/N373C}$ mutant was buffer-exchanged into 20 mM Tris·HCl (pH 8.0) and 100 mM NaCl by using a Micro-Spin column and then incubated with 10 μM copper-1,10-phenantroline for 3 h at 37 °C, before 5 mM EDTA was added to stop the reaction. Disulfide-bond formation was analyzed by changes in electrophoretic mobility following nonreducing SDS/PAGE.

Assays. Cleavage of Mca-AKVYPYPME-Dpa(Dnp)-amide by 20S in the presence or the absence of Cdc48 was assayed at 45 °C as described, except that DDT was omitted from the reaction (8). For peptidase assays in the presence of ADP·AlF$_4^-$, 2 mM Al(NO$_3$)$_3$, and 12 mM NaF were added to reaction buffer that contained 2 mM ADP and were preincubated for 20 min before starting the reaction by adding peptide. ATP hydrolysis was measured by a NADH-coupled colorimetric assays in the presence of an ATP-regeneration system (10 U·mL^{-1} pyruvate kinase, 10 U·mL^{-1} lactate dehydrogenase, 1 mM NADH, and 7.5 mM phosphoenolpyruvate) and 5 mM ATP. Reactions were performed in 30 μL of PD buffer (20 mM Hepes–KOH, pH 7.5, 100 mM KCl, 20 mM MgCl$_2$) with 0.3 μM Cdc48 variants at 45 °C. Reaction components were preincubated at 45 °C for 20 min before starting reactions by adding ATP. Protein unfolding was measured by changes in photo-cleaved Kaede-ssrA fluorescence (excitation, 540 nm; emission, 580 nm) at 45 °C in 50 mM Hepes–KOH, 100 mM KCl, 20 mM MgCl$_2$, 5 mM ATP, and an ATP-regenerating system (20 U·mL^{-1} pyruvate kinase; 15 mM phosphoenolpyruvate). Reaction components were preincubated for 20 min before starting the unfolding reactions by adding ATP. Protein degradation was measured by the loss of ^{SF}GFP-ssrA fluorescence (excitation, 467 nm; emission, 511 nm) in the presence of 0.9 μM 20S peptidase with 0.3 μM Cdc48 variants or with 0.3 μM ^{x}Cdc48–20S or ^{x}Cdc48$^{\Delta N}$–20S complexes as described above.

The accessibility of the C-terminal cysteine residue in the HbYX motif of Cdc48$^{*/L745C}$ was probed by measuring the reaction kinetics of modification with DTNB by increases in absorption at 412 nm. Cdc48$^{*/L745C}$ (10 μM) was incubated at 45 °C in PD buffer with 5 mM ATP or ADP, and reactions were started by adding 0.1 mM DTNB. Rates were also determined for trypsin-digested Cdc48$^{*/L745C}$ to ensure full accessibility of the HbYX tails and for DTNB hydrolysis in reaction buffer alone.

Single-Particle EM Data Collection and Analysis. ^{x}Cdc48–20S or ^{x}Cdc48$^{\Delta N}$–20S complexes (30 nM) were incubated in 5 mM ATP for 10 min at 45 °C, before being negatively stained with uranyl acetate [1% (wt/vol)] on continuous carbon-film grids. Electron micrographs of single particles were recorded by using a 2K × 2K CCD camera on a JEOL JEM-2100F electron microscope at 200 KeV, 30,000× nominal magnification. For ^{x}Cdc48–20S, 4,724 particles were collected in 183 CCD images. For ^{x}Cdc48$^{\Delta N}$–20S, 5,260 particles were collected in 101 images. In both datasets, the imaging defocus range was between 1.5 and 2.5 μm. Particle images were boxed and 2×-binned to 7.05 Å per pixel. Because of their elongated shape, almost all of the particles assumed side views in images. Each dataset was subjected to direct classification, a reference-free and alignment-free classification function (described in more detail below) in the PARTICLE software package (www.sbgrid.org/software/title/PARTICLE). A total of 2,820 classes were identified for ^{x}Cdc48–20S, and 4,880 classes were identified for ^{x}Cdc48$^{\Delta N}$–20S.

Because all particle images were side views, their common lines were mostly coaxially aligned and poorly suited for ab initio angular reconstitution. We therefore resorted to tomographic imaging and single-particle tomogram averaging to create an initial 3D model for the ^{x}Cdc48$^{\Delta N}$–20S complex. The tomographic data were collected on an FEI T12 electron microscope, and the tilt-series coverage was from −30° to +30° at intervals of 2°. The relatively small tilting range was used to avoid imaging artifacts from staining at high-tilt angles, while the adverse missing-wedge effect was mitigated by the intrinsic symmetry of the assembly. A total of 28 single-particle tomograms were collected, from which 4 particles with the Cdc48–20S axial direction closely aligned to the tilt axis were selected for tomogram averaging after applying C6- and C7-symmetrization in the Cdc48 and 20S regions, respectively. The resulting density map served as the initial reference for the single-particle 3D reconstruction and refinement for both the ^{x}Cdc48$^{\Delta N}$–20S and ^{x}Cdc48–20S datasets.

In each case, class-averaged particle images [with enhanced signal-to-noise ratio (SNR)] were manually pruned to remove the Cdc48–20S assemblies that were not coaxially aligned, or the N domain was disordered in the case of full-length construct (<10% of the total classes). The remaining class averages—2,612 for ^{x}Cdc48–20S and 4,575 for ^{x}Cdc48$^{\Delta N}$–20S—were first aligned to the initial reference by an exhaustive projection-matching search (C1; no symmetry assumption) within 30° from the axial direction. The density map derived from the aligned class averages then served as the new reference for the subsequent iterative refinement. Once the process converged, the alignment parameters of the class-average images were assigned to the respective seed image (defined in the direct particle classification algorithm; *A Direct Method for 2D Classification in Single-Particle EM*) of the class for the final round of refinement and 3D reconstruction. The resolution was measured at ~39 Å for the ^{x}Cdc48$^{\Delta N}$–20S density map and ~42 Å for the ^{x}Cdc48–20S density map. The resolution measurement and the Euler-angle distribution of both reconstructions are plotted in Fig. S4. The electron-density maps for ^{x}Cdc48–20S and ^{x}Cdc48$^{\Delta N}$–20S have been deposited to the EMDataBank (accession codes EMD-5923 and EMD-5924, respectively).

A Direct Method for 2D Classification in Single-Particle EM. In ab initio single-particle 3D reconstruction, an initial model is first derived either by common-line-based angular reconstitution or by the random-conical-tilt technique. In both ab initio methods, particle 2D classification assumes a pivotal role in identifying distinct projection views and enhancing the image SNR via in-class averaging. In the conventional approach of 2D classification, particle images are first aligned to establish pixel registration across all frames, which are then subjected to principal component analysis (PCA) and clustering in a reduced eigenspace. To align the particles, the target functions frequently rely on the cross-correlation (CC) between the particle image and a set of references. However, because CC often produces spurious peaks under the noise typical in EM images, erroneous alignments often lead to false classification and ultimately low-resolution or even incorrect model reconstruction. To overcome the uncertainty induced by low SNR in particle alignment and classi-

cation, one of us (J.Z.C.) developed a "direct particle classification" (DPC) technique that eliminates image registration in the process.

The objective of particle 2D classification is to produce SNR-enhanced projection views, from which 3D reconstruction can proceed. In the conventional practice, particles are partitioned into a small number of classes, and the class averages represent the most popular projections. This goal can also be achieved by an orthogonal approach on an individual basis by formulating the task as: "For each particle image, what others in the dataset agree with it?" In contrast to the class-centric "group consensus," the particle-centric approach focuses on analyzing the conformational variation around each image instance. The algorithm proceeds as follows:

1. For each particle p in the data stack, systematically translate and rotate the image at discrete steps of pixel precision that enumerate the complete 2D-alignment parameter space (Fig. S5A). For instance, given a particle of 30 pixels in diameter approximately centered in a 64 × 64-pixel image, at 3° rotational steps and ±10 pixels translations in X/Y of the frame, each image will generate 120 × 21 × 21 = 52,920 distinct transformations. As a result, the original stack $\{p\}$ is expanded by 52,920 times to $\{p^x\}$, and the data expansion eliminates the need for particle alignment. From here on, p will be referred to as "the original particle" before synthetic-image transformation.

2. Apply pixel-based PCA directly on the expanded $\{p^x\}$ and construct a reduced eigenspace. Then, decompose all images of $\{p^x\}$ in the eigenspace and identify a tight cluster centered around each original particle p. This cluster will be referred to as "the class seeded by p" and is denoted as $C(p)$. At this stage, there are as many seeded classes as the number of original particles in $\{p\}$, and each class contains at least one member, the seed itself.

3. Class pruning via "mutual inclusion" (Fig. S5B): For two original particles p, q and their transformed images p^t, q^T (where t and T are inversely related), if $p^t \in C(q)$ but $q^T \notin C(p)$, then p^t is removed from $C(q)$. After pruning, the mutual inclusion of class seeds is guaranteed: If $p^t \in C(q)$, then $q^T \in C(p)$. The mutual inclusion between p and q requires close proximity of both (p^t, q) and (q^T, p) in the reduced eigenspace, and therefore enforces the stability and reliability of the resulting classes.

In the application to the classification of Cdc48–20S particles—which are ~24 nm in the longest dimension and boxed into 64 × 64 frames at 7.05 Å per pixel—3° rotations and ± 10-pixel maximal translations were used in the systematic data expansion to ensure pixel precision. Ultimately, 2,820 classes (with 32 particles per class on average) were identified for the ^{x}Cdc48–20S dataset, and 4,880 classes (with 39 particles per class on average) were identified for the ^{x}Cdc48$^{\Delta N}$–20S dataset.

Unlike conventional classification methods that partition a particle stack into a much smaller number of groups, DPC creates one class for each original particle, from which the stability of the class can be assessed via the agreement between classes and among the class members. Unstable classes, which are often seeded by false particles or contaminants with low membership, are then rejected. As a result, the total number of classes is determined through algorithmic pruning instead of by often ambiguous and subjective user request.

The DPC function has been implemented in the PARTICLE package that is available for public access on SBGrid (www.sbgrid.org/software/title/PARTICLE). The performance of DPC has been validated on public benchmarks provided by the National Resource for Automated Molecular Microscopy at The Scripps Research Institute.

1. Finley D (2009) Recognition and processing of ubiquitin-protein conjugates by the proteasome. *Annu Rev Biochem* 78:477–513.
2. Voges D, Zwickl P, Baumeister W (1999) The 26S proteasome: A molecular machine designed for controlled proteolysis. *Annu Rev Biochem* 68:1015–1068.
3. Groll M, et al. (2000) A gated channel into the proteasome core particle. *Nat Struct Biol* 7(11):1062–1067.
4. Kish-Trier E, Hill CP (2013) Structural biology of the proteasome. *Annu Rev Biophys* 42:29–49.
5. Maupin-Furlow J (2012) Proteasomes and protein conjugation across domains of life. *Nat Rev Microbiol* 10(2):100–111.
6. Sauer RT, Baker TA (2011) AAA+ proteases: ATP-fueled machines of protein destruction. *Annu Rev Biochem* 80:587–612.
7. Barthelme D, Sauer RT (2013) Bipartite determinants mediate an evolutionarily conserved interaction between Cdc48 and the 20S peptidase. *Proc Natl Acad Sci USA* 110(9):3327–3332.
8. Barthelme D, Sauer RT (2012) Identification of the Cdc48·20S proteasome as an ancient AAA+ proteolytic machine. *Science* 337(6096):843–846.
9. Baek GH, et al. (2013) Cdc48: A Swiss army knife of cell biology. *J Amino Acids* 2013: 183421.

Barthelme et al.

10. Allers T, Barak S, Liddell S, Wardell K, Mevarech M (2010) Improved strains and plasmid vectors for conditional overexpression of His-tagged proteins in *Haloferax volcanii*. *Appl Environ Microbiol* 76(6):1759–1769.

11. DeLaBarre B, Brunger AT (2003) Complete structure of p97/valosin-containing protein reveals communication between nucleotide domains. *Nat Struct Biol* 10(10):856–863.

12. Walz J, et al. (1998) 26S proteasome structure revealed by three-dimensional electron microscopy. *J Struct Biol* 121(1):19–29.

13. Smith DM, et al. (2005) ATP binding to PAN or the 26S ATPases causes association with the 20S proteasome, gate opening, and translocation of unfolded proteins. *Mol Cell* 20(5):687–698.

14. Smith DM, Fraga H, Reis C, Kafri G, Goldberg AL (2011) ATP binds to proteasomal ATPases in pairs with distinct functional effects, implying an ordered reaction cycle. *Cell* 144(4):526–538.

15. Matyskiela ME, Lander GC, Martin A (2013) Conformational switching of the 26S proteasome enables substrate degradation. *Nat Struct Mol Biol* 20(7):781–788.

16. Rouiller I, et al. (2002) Conformational changes of the multifunction p97 AAA ATPase during its ATPase cycle. *Nat Struct Biol* 9(12):950–957.

17. Tang WK, et al. (2010) A novel ATP-dependent conformation in p97 N-D1 fragment revealed by crystal structures of disease-related mutants. *EMBO J* 29(13):2217–2229.

18. DeLaBarre B, Brunger AT (2005) Nucleotide dependent motion and mechanism of action of p97/VCP. *J Mol Biol* 347(2):437–452.

19. Gerega A, et al. (2005) VAT, the thermoplasma homolog of mammalian p97/VCP, is an N domain-regulated protein unfoldase. *J Biol Chem* 280(52):42856–42862.

20. Förster A, Masters EI, Whitby FG, Robinson H, Hill CP (2005) The 1.9 A structure of a proteasome-11S activator complex and implications for proteasome-PAN/PA700 interactions. *Mol Cell* 18(5):589–599.

21. Rockel B, et al. (1999) Structure of VAT, a CDC48/p97 ATPase homologue from the archaeon *Thermoplasma acidophilum* as studied by electron tomography. *FEBS Lett* 451(1):27–32.

22. Rockel B, Jakana J, Chiu W, Baumeister W (2002) Electron cryo-microscopy of VAT, the archaeal p97/CDC48 homologue from *Thermoplasma acidophilum*. *J Mol Biol* 317(5):673–681.

23. Niwa H, et al. (2012) The role of the N-domain in the ATPase activity of the mammalian AAA ATPase p97/VCP. *J Biol Chem* 287(11):8561–8570.

24. Beckwith R, Estrin E, Worden EJ, Martin A (2013) Reconstitution of the 26S proteasome reveals functional asymmetries in its AAA+ unfoldase. *Nat Struct Mol Biol* 20(10):1164–1172.

25. Wendler P, et al. (2009) Motor mechanism for protein threading through Hsp104. *Mol Cell* 34(1):81–92.

26. Haslberger T, et al. (2008) Protein disaggregation by the AAA+ chaperone ClpB involves partial threading of looped polypeptide segments. *Nat Struct Mol Biol* 15(6):641–650.

27. Glynn SE, Nager AR, Baker TA, Sauer RT (2012) Dynamic and static components power unfolding in topologically closed rings of a AAA+ proteolytic machine. *Nat Struct Mol Biol* 19(6):616–622.

28. Nager AR, Baker TA, Sauer RT (2011) Stepwise unfolding of a β barrel protein by the AAA+ ClpXP protease. *J Mol Biol* 413(1):4–16.

29. Yu Y, et al. (2010) Interactions of PAN's C-termini with archaeal 20S proteasome and implications for the eukaryotic proteasome-ATPase interactions. *EMBO J* 29(3):692–702.

30. Dombkowski AA (2003) Disulfide by Design: A computational method for the rational design of disulfide bonds in proteins. *Bioinformatics* 19(14):1852–1853.

31. Stadtmueller BM, et al. (2010) Structural models for interactions between the 20S proteasome and its PAN/19S activators. *J Biol Chem* 285(1):13–17.

www.manaraa.com